


## Accurately Estimating Redshifts from CSST Slitless Spectroscopic Survey using Deep Learning

XINGCHEN ZHOU,<sup>1,2</sup> YAN GONG <sup>1,3,2</sup>, XIN ZHANG,<sup>1,2</sup> NAN LI,<sup>1,2</sup> XIAN-MIN MENG,<sup>1,2</sup> XUELEI CHEN,<sup>1,2,4</sup> RUN WEN,<sup>5,6</sup>  
YUNKUN HAN,<sup>7</sup> HU ZOU,<sup>1</sup> XIAN ZHONG ZHENG,<sup>5,6</sup> XIAOHU YANG,<sup>8,9</sup> HONG GUO,<sup>10</sup> AND PENGJIE ZHANG<sup>8,9</sup>

<sup>1</sup>National Astronomical Observatories, Chinese Academy of Sciences, 20A Datun Road, Beijing 100101, People's Republic of China

<sup>2</sup>Science Center for China Space Station Telescope, National Astronomical Observatories, Chinese Academy of Sciences, 20A Datun Road, Beijing 100101, People's Republic of China

<sup>3</sup>University of Chinese Academy of Sciences, Beijing, 100049, People's Republic of China

<sup>4</sup>Centre for High Energy Physics, Peking University, Beijing 100871, Peoples Republic of China

<sup>5</sup>Purple Mountain Observatory, Chinese Academy of Sciences, 10 Yuanhua Road, Nanjing 210023, People's Republic of China

<sup>6</sup>School of Astronomy and Space Sciences, University of Science and Technology of China, Hefei, 230026, People's Republic of China

<sup>7</sup>Yunnan Observatories, Chinese Academy of Sciences, 396 Yangfangwang, Guandu District, Kunming 650216, People's Republic of China

<sup>8</sup>Department of Astronomy, School of Physics and Astronomy, Shanghai Jiao Tong University, Shanghai 200240, People's Republic of China

<sup>9</sup>Tsung-Dao Lee Institute and Key Laboratory for Particle Physics, Astrophysics and Cosmology, Ministry of Education, Shanghai 201210, People's Republic of China

<sup>10</sup>Shanghai Astronomical Observatory, Chinese Academy of Sciences, Shanghai 200030, People's Republic of China

### ABSTRACT

China Space Station Telescope (CSST) has the capability to conduct slitless spectroscopic survey simultaneously with photometric survey. The spectroscopic survey will measure slitless spectra, potentially providing more accurate estimations of galaxy properties, particularly redshift, compared to broadband photometry. However, due to low-resolution and signal-to-noise ratio of slitless spectra, measurement of these properties is significantly challenging. In this study, we employ a Bayesian neural network (BNN) to assess the accuracy of redshift estimations from slitless spectra anticipated to be observed by CSST. The slitless spectra are simulated based on real data from the early data release of the Dark Energy Spectroscopic Instrument (DESI-EDR) and the 16th data release of the Baryon Oscillation Spectroscopic Survey (BOSS-DR16), combining the 9th data release of the DESI Legacy Survey (DESI LS DR9). The BNN provides redshifts estimates along with corresponding uncertainties, achieving an accuracy of  $\sigma_{\text{NMAD}} = 0.00063$ , outlier percentage  $\eta = 0.92\%$  and weighted mean uncertainty  $\bar{E} = 0.00228$ . These results successfully meet the requirement for cosmological studies using slitless spectra from CSST.

*Keywords:* galaxies: distances and redshifts — cosmology: observations — techniques: spectroscopic

### 1. INTRODUCTION

Redshifts are one of the fundamental quantities for studying galaxies. The most accurate redshifts are determined through observing and analyzing high-resolution spectra from galaxies. However, obtaining high-resolution spectra is a time-consuming task, especially for high-redshift and faint sources, which require hours of observation to successfully measure their redshifts. As a result, photometric redshifts, estimated

from several photometric measurements, become a necessary option for most sources observed in ongoing and future cosmological surveys. However, the large error of  $\gtrsim 0.02$  associated with photometric redshifts severely hinders certain cosmological studies using techniques such as baryon acoustic oscillation (BAO, Bassett & Hlozek (2010)) and redshift-space distortions (RSD, Hamilton (1998)). To match the accuracy required by these cosmological studies and the survey speed of current photometric surveys, a compromise solution exists: slitless spectra. Slitless spectra represent a category of low-resolution spectroscopy performed without a narrow slit, which typically allows only light from a small region to

be diffracted. Current and future photometric surveys, such as Euclid Space Telescope (Euclid, [Euclid Collaboration et al. \(2024\)](#)), James Webb Space Telescope (JWST, [Sabelhaus & Decker \(2004\)](#)), Nancy Grace Roman Space Telescope (Roman) <sup>1</sup> and China Space Station Telescope (CSST, [Zhan \(2018\)](#); [Gong et al. \(2019\)](#)), all include modules to observe slitless spectra for galaxies.

CSST is a 2-meter space telescope designed for photometric observations across seven bands, ranging from near-ultraviolet to near-infrared. The slitless spectroscopy module, which include three bands (*GU*, *GV* and *GI*), operates alongside the photometric module, enabling simultaneous photometric and slitless spectroscopic observations. These three bands can reach  $5\sigma$  magnitude limit of 23.2, 23.4 and 23.2 for point sources, respectively, with a low spectroscopic resolution of each band as  $R = \lambda/\Delta\lambda \geq 200$  ([Gong et al. 2019](#)). For extended sources such as galaxies, slitless spectra can be significantly affected by observational and instrumental effects, challenging the one-dimensional spectrum extraction procedure and thus resulting in low-resolution and signal-to-noise ratio (SNR) spectra. These challenges make the recognition of emission and absorption lines, breaks, and other spectroscopic features difficult. As a result, galaxy properties such as redshift and line fluxes estimated from these spectra can be highly inaccurate, leading to errors comparable to those derived from broadband photometry. Addressing the challenge of successfully measuring these galaxy properties from such low-resolution and SNR slitless spectra remains an urgent problem.

Machine Learning (ML), particularly Deep Learning (DL) algorithms (also known as neural networks), offers a potential solution to the challenges posed by noisy data. This algorithm can effectively learn the inherent correlations between inputs and outputs using large datasets, making them well-suited to handle data significantly affected by instrumental or other forms of noise. In the astronomical and cosmological communities, neural networks have gained prominence in recent years, achieving applications across various fields. The multilayer perceptron (MLP), a simple neural network, has been applied to estimate photometric redshifts from multi-band photometric measurements ([Collister & Lahav 2004](#); [Sadeh 2014](#); [Zhou et al. 2022a](#)), surpassing the accuracy achieved by traditional spectral energy distribution (SED) fitting methods.

Furthermore, state-of-the-art convolutional neural networks (CNN, [Lecun et al. \(1998\)](#)), which excel in directly processing images, have become indispensable in astronomical and cosmological analysis. Applications include deriving photometric redshifts or other quantities from galaxy images ([Pasquet et al. 2019](#); [Henghes et al. 2022](#); [Zhou et al. 2022a](#); [Tewes et al. 2019](#); [Zhang et al. 2024](#)), discovering strong lensing systems or mergers ([He et al. 2020](#); [Schaefer et al. 2018](#); [Li et al. 2020](#); [Rezaei et al. 2022](#); [Pearson et al. 2019](#); [Arendt et al. 2024](#)), and constraining cosmological parameters from large-scale structures or weak gravitational lensing ([Pan et al. 2020](#); [Min et al. 2024](#); [Hortúa et al. 2023](#); [Gupta et al. 2018](#); [Fluri et al. 2022](#)).

In addition to processing 2-dimensional arrays, CNNs can be adapted to handle 1-dimensional sequences or 3-dimensional data cubes. Spectra are 1-dimensional sequences containing redshift or other information, which can be effectively extracted by 1d-CNNs. The application of 1d-CNNs for deriving redshifts from spectra is extensively researched ([Rastegarnia et al. 2022](#); [Busca & Balland 2018](#)).

Unlike traditional fitting methods that produce both redshifts and uncertainties, deep learning methods typically provide only redshift values. Recognizing the importance of uncertainties in cosmological studies, Bayesian neural networks (BNN) ([MacKay 1995](#); [Blundell et al. 2015](#); [Gal & Ghahramani 2015](#)), which can output both point estimations and uncertainties, have gained significant attention. By assigning probability distributions to each weight in the network, BNNs can capture and propagate uncertainties from data and neural network itself to the output, providing not only point predictions but also confidence intervals or posterior distributions.

Although deep learning algorithm offers advantages in providing better accuracy, higher speed, and direct processing of raw data, several challenges need careful consideration. Since deep learning models heavily rely on training data, obtaining abundant and representative data for observation is a primary concern. Specifically, for redshift estimation, a large dataset with high-quality spectroscopic redshifts is essential. Fortunately, several ongoing and planned spectroscopic surveys, such as the Dark Energy Spectroscopic Instrument (DESI, [DESI Collaboration et al. \(2016\)](#)), Prime Focus Spectrograph (PFS, [Tamura et al. \(2016\)](#)), Multiplexed Spectroscopic Telescope (MUST) <sup>2</sup>, MegaMapper ([Schlegel et al. 2022](#)) and Wide-field Spectroscopic

<sup>1</sup> <https://roman.gsfc.nasa.gov/>

<sup>2</sup> <https://must.astro.tsinghua.edu.cn/en>

Telescope (WST, Mainieri et al. (2024)), aim to observe a substantial number of galaxy spectra with accurate redshifts. Including completed surveys like zCOSMOS (Lilly et al. 2007), VIMOS-VLT Deep Survey (VVDS, Le Fevre et al. (2013)), Sloan Digital Sky Survey (SDSS, Ahumada et al. (2020)), Baryon Oscillation Spectroscopic Survey (BOSS, Dawson et al. (2013)), a sufficient and representative training set for redshift estimation can be achieved.

In this work, we generate slitless spectra expected to be observed by CSST based on real spectroscopic observations. Considering the redshift coverage and survey fields, we employ data from DESI early data release (DESI-EDR, DESI Collaboration et al. (2023)) and BOSS 16th data release (BOSS-DR16, Dawson et al. (2013)). DESI-EDR has made available 1.2 million high-resolution spectra of galaxies and quasars collected during the Survey Validation (SV) phase for target selections. Since the number of sources in DESI-EDR are limited, we supplement our slitless spectrum dataset with BOSS data, which shares a similar pipeline for the measurement of spectroscopic redshifts, to increase the data size for training the neural network model. After obtaining the slitless spectra, we train a 1d-BNN with these spectra and their corresponding accurate spectroscopic redshifts, and then analyze the redshift accuracy that can be achieved for CSST slitless spectroscopic survey.

The structure of this paper is organized as follows: we briefly describe CSST slitless spectra simulation software and then explain the generation of the mock slitless spectra in Section 2. And the neural network methods including CNN and BNN are introduced in Section 3. Then we demonstrate our results in Section 4. Finally, this paper is concluded in Section 5.

## 2. MOCK DATA

In this section, we firstly introduce the slitless spectra simulation software in CSST data analysis pipeline, and then explain the data generation procedure of slitless spectra using this software from real spectroscopic observations.

### 2.1. Slitless spectra simulation software

The simulation software for slitless spectra is an integral part of the CSST data analysis pipeline, with the code available online<sup>3</sup>. We provide a brief overview of the workflow here, and interested readers are recommended to consult Zhang et al. (in preparation) for

detailed information. This software utilizes spectral energy distributions (SEDs) and morphological parameters of galaxies to generate mock spectra. Initially, the dispersion curve for the grating is determined through a fitting process that considers the spectroscopic properties of the CSST’s slitless spectrum. Following this, the energy profile of the galaxy, which is contingent upon its morphological parameters, is converted into a pixelated galaxy image. Each pixel of the galaxy image undergoes dispersion based on the dispersion curve specific to the CSST grating, in conjunction with the sensitivity curve of the CSST instrument and the galaxy’s SED. Finally, all dispersed components are integrated into a two-dimensional slitless spectral image. Additionally, instrumental effects are simulated using a point spread function (PSF), assumed to be 2D Gaussian distribution with a full width at half maximum (FWHM) of  $0.3''$ . The sky backgrounds, including zodiacal and earthshine components, are computed as  $0.019, 0.214, 0.329 \text{ e}^{-\text{s}^{-1}}\text{pixel}^{-1}$  for the *GU*, *GV* and *GI* bands respectively. To mitigate the effects of instrumental and background noise, we co-add spectra from four exposures, each with a duration of 150 seconds. Following these procedures, we generate first-order spectral images expected to be observed by CSST, from which we can extract the 1d-spectra and the corresponding errors.

### 2.2. Data generation

To realistically simulate our slitless spectra, we utilize spectroscopic observations from the Dark Energy Spectroscopic Instrument (DESI) and the Baryon Oscillation Spectroscopic Survey (BOSS). DESI is an ongoing spectroscopic survey conducted on the Mayall 4-meter telescope at Kitt Peak National Observatory. Over its 5-year mission, DESI aims to observe spectra for more than 30 million galaxies and quasars across 14,000 square degrees of sky (DESI Collaboration et al. 2016). Recently, DESI has released its Early Data Release (EDR), which includes spectroscopic data for 1.8 million targets observed during the Survey Validation (SV) phase conducted from December 2020 to June 2021 (DESI Collaboration et al. 2023).

We select sources from the EDR spectroscopic redshift catalogue using the following criteria:

$$\begin{aligned}
 \text{SV\_PRIMARY} &== \text{True} \\
 \text{MASKBITS} &== 0 \\
 \text{SPECTYPE} &== \text{GALAXY} \\
 \text{ZWARN} &== 0 \\
 \text{FLUX\_G, R, Z} &> 0 \\
 \text{FLUX\_IVAR\_G, R, Z} &> 0 \\
 \text{MORPHTYPE} &!= \text{PSF}
 \end{aligned} \tag{1}$$

<sup>3</sup> [https://csst-tb.bao.ac.cn/code/zhangxin/sls\\_1d\\_spec](https://csst-tb.bao.ac.cn/code/zhangxin/sls_1d_spec)

Here, SV\_PRIMARY indicates the best recommended redshift if the same source appears multiple times in the catalogue, while MASKBITS is the bitwise mask indicating that the source touches a pixel in a masked area. SPECTYPE and ZWARN are source classification and indicators of potential issues in spectroscopic redshift measured by Redrock<sup>4</sup>, a commonly used redshift fitting software. We further control the quality of sources by applying constraints on photometric measurements in the  $g$ ,  $r$  and  $z$  bands of the DESI legacy imaging survey (Dey et al. 2019). MORPHTYPE indicates the Tractor model used to fit the source during photometric measurement. This constraint ensures that the selected sources are extended, allowing for accurate morphological parameter measurements. It should be noted that some PSF sources are spectroscopically classified as galaxies. These PSF models are assigned probably due to the resolution of  $\sim 1.0''$  in imaging data of DESI legacy survey, and we simply exclude these galaxies in our dataset. To obtain the morphological parameters required to derive our slitless spectra, we match the selected sources with the sweep catalogue of DESI legacy survey DR9<sup>5</sup> and retrieve the morphological parameters, including effective radius  $r_{\text{eff}}$ , sersic index  $n$ , two ellipticity components  $\epsilon_1, \epsilon_2$  and their variance. And we perform another selection to filter the sources with valid morphological measurements:

$$\begin{aligned} \text{SHAPE\_R} &> 0 \\ \text{SHAPE\_IVAR\_R} &> 0 \\ \text{SHAPE\_E1\_IVAR} &> 0 \\ \text{SHAPE\_E2\_IVAR} &> 0 \\ \text{SERSIC\_IVAR} &> 0 \end{aligned} \quad (2)$$

and then we calculate the axis ratio  $b/a$  and position angle  $\phi$  using the following equations as recommended by DESI:

$$\begin{aligned} |\epsilon| &= \sqrt{\epsilon_1^2 + \epsilon_2^2}, \\ \frac{b}{a} &= \frac{1 - |\epsilon|}{1 + |\epsilon|}, \\ \phi &= \frac{1}{2} \arctan \frac{\epsilon_2}{\epsilon_1}. \end{aligned} \quad (3)$$

This selection process results in approximately 180,000 sources with high-quality spectroscopic redshifts. Note that we admit that the morphological parameters of some sources have large errors, exerting significant effects on simulated slitless spectra. However, these ef-

fects are ignored in this work since our aim is to estimate redshifts and the relation between the spectra and redshifts is well-determined regardless of the morphological errors.

After obtaining the redshifts and morphological parameters, the next step involves acquiring the spectral energy distribution (SED) for each source to simulate slitless spectra. The spectroscopic redshifts of the sources have been determined using model spectra fitted by Redrock, and all redshift warning flags are zero, indicating no issues with the fitting process. This allows us to use the model spectra to accurately represent the SED of each source. These model spectra can be constructed using the COEFF provided in the DESI-EDR catalogue, combining Redrock templates, or accessed via the Spectra Analysis & Retrieval Catalog Lab (SPARCL)<sup>6</sup>. The model spectra obtained through both approaches are the same, and we choose the latter.

The 180,000 sources selected from DESI-EDR are insufficient for training our neural network to derive redshifts from low-quality slitless spectra. To supplement our dataset, we utilize data from the Baryon Oscillation Spectroscopic Survey (BOSS). BOSS is a spectroscopic survey primarily targeting luminous red galaxies (LRGs) up to  $z \sim 0.7$  and quasars (QSOs) at redshifts  $2.2 < z < 3$ , aimed at detecting the characteristic scale imprinted by baryon acoustic oscillations (BAO) in the early Universe. Over its 5-year observation period, BOSS has measured spectra for approximately 4 million sources, covering 10,000 square degrees (Dawson et al. 2013). For this work, we use 16th data release from BOSS (BOSS-DR16).

Similar to our approach with DESI data, we select galaxies with a spectroscopic redshift warning ZWARN == 0, produced by Redrock software, and match these sources with the DESI LS DR9. We exclude sources modeled as PSF and without reasonable photometric measurements in the  $g$ ,  $r$  and  $z$  bands and those lacking valid morphological parameters. This results in a selection of 450,000 galaxies, for which we download their model spectra using SPARCL. In total, we obtain approximately 600,000 sources.

The spectroscopic redshift distributions are illustrated in Figure 1. We notice that most sources from DESI-EDR are at low redshifts, while high redshift sources up to  $z \sim 1$  are supplemented by BOSS-DR16. The distribution of morphological parameters, including effective radius  $r_{\text{eff}}$ , sersic index  $n$ , axis ratio  $b/a$  and position angle  $\phi$  are illustrated in Figure 2. Notably, galaxies

<sup>4</sup> <https://github.com/desihub/redrock>

<sup>5</sup> <https://www.legacysurvey.org/dr9/files/#sweep-catalogs-region-sweep>

<sup>6</sup> <https://astrosparcl.datalab.noirlab.edu/>

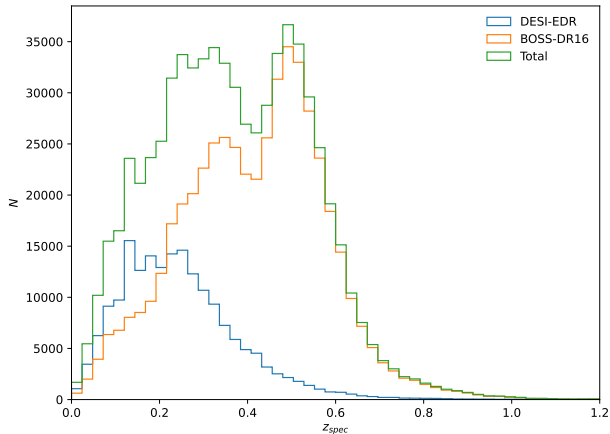


**Figure 1.** Spectroscopic redshift distributions for selected sources in DESI-EDR, BOSS-DR16 and total.

with a Sersic index of 6 dominate, particularly those from BOSS-DR16. This selection bias is as expected, as the Sersic index positively correlates with galaxy size and luminosity. Hence, for valid morphological measurements and accurate spectroscopic redshift extraction, the sources tend to be larger in size and brighter in luminosity.

After obtaining the model spectra and morphological parameters for sources in DESI-EDR and BOSS-DR16, we simulate the slitless spectra using the simulation software mentioned in Section 2.1. The signal-to-noise ratio (SNR) of the simulated CSST slitless spectra in  $GU$ ,  $GV$ ,  $GI$  and total are illustrated in Figure 3. We notice that the SNRs of  $GI$  are the best reaching a peak at about 2, while most SNRs of  $GU$  and  $GV$  bands are lower than 1. Additionally, the total SNRs of these spectra peak at  $\sim 1$ , indicating signal and noise are at similar level. In Figure 4, we display two examples of simulated first-order slitless spectral images in  $GU$ ,  $GV$  and  $GI$  bands, and the corresponding extracted one-dimensional spectra are shown in Figure 5. The SEDs used in simulation are also illustrated and they are in consistency with the spectra. Additionally, the source information including coordinates (R.A. and Dec.), spectroscopic redshifts, morphological parameters used in simulation and SNR in  $GU$ ,  $GV$  and  $GI$  band are also shown. For the low-redshift source in the left panel, we can clearly recognize the dispersed 2d-spectra in  $GV$  and  $GI$  bands, and SNRs of the extracted 1d-spectra in these two bands are relatively high. While for high-redshift source in the right panel, only a faint 2d-spectra in  $GI$  band can be recognized, with the other two bands are dominated by noise, hence the extracted 1d-spectra are correspondingly with

low SNR. Overall, the slitless spectra are severely affected by background and instrumental noise and the recognition of spectroscopic features such as break, absorption and emission lines is difficult, leading to challenges for successful redshift determinations using traditional approaches such as spectrum fitting or feature identification.

### 3. METHODOLOGY

We employ deep neural network to extract redshifts from slitless spectra expected to be observed by CSST. To satisfy the requirement of some cosmological studies, we further construct Bayesian neural network to derive redshift values along with their uncertainties.

#### 3.1. Neural networks

Since spectra are 1-dimensional sequences, we employ 1d-CNN to process them. CNN is a powerful deep learning model which can learn the internal connections between data and labels. Therefore, we expect that our 1d-CNN can learn the mapping between slitless spectra and redshifts. To improve its learning ability, we increase the depth of our 1d-CNN using ResNet blocks (He et al. 2015). This block can effectively reduce the vanishing gradient problem commonly happened in deep neural networks through skip connections, as illustrated in the right panel of Figure 6. The convolutional layer in skip connection is applied when this block process and down-sample the features at the same time. Following Zhou et al. (2021), the input to our CNN includes spectra and corresponding errors as a two-channel sequences. And then the inputs are processed by one convolutional layer with 32 kernels with kernel size of 7, followed by a max-pooling to reduce the feature dimension. After this shallow feature extraction layers, we structure 8 ResNet blocks to obtain useful features from spectra and further reduce the feature dimension. The 1d convolutional layers in these blocks are all followed by BatchNormalization layers (Ioffe & Szegedy 2015) to reduce overfitting. And ReLU activation functions (Agarap 2018) are structured to apply non-linearity. Subsequently, the features are vectorized to one-dimension using global average pooling, and then a dropout layer (Srivastava et al. 2014) with drop rate of 0.2 is applied. This dropout layer also functions as overfitting reduction. Finally, the output layer with one neuron is structured. The illustration of architecture is displayed in the left panel of Figure 6.

The neural network mentioned yet can only output redshift value. In order to output redshifts along with their uncertainties, we construct a Bayesian neural network that captures both the epistemic and aleatoric uncertainties arise from neural network model and dataset



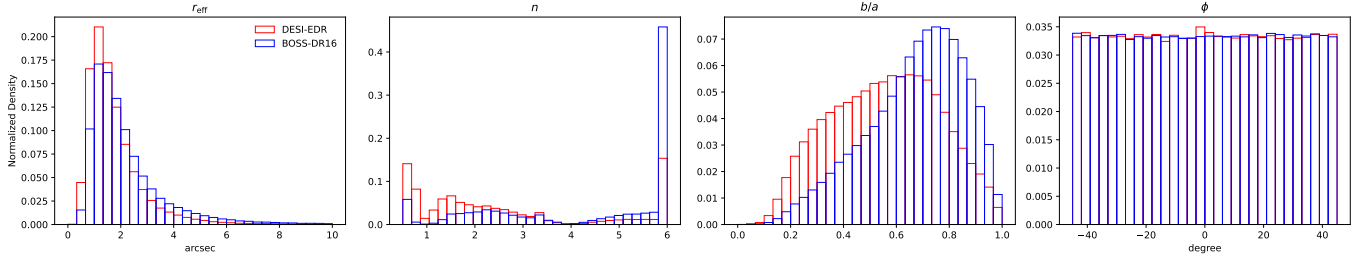


**Figure 2.** The distribution of four morphological parameters: effective radius  $r_{\text{eff}}$ , seric index  $n$ , axis ratio  $b/a$  and position angle  $\phi$  of sources from DESI-EDR and BOSS-DR16.

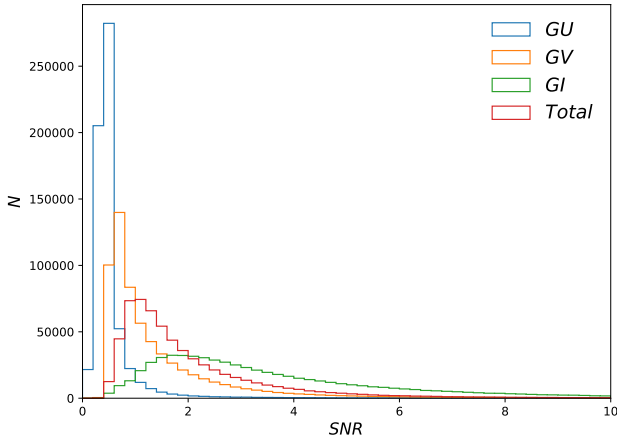


**Figure 3.** The SNR distributions of simulated slitless spectra in  $GU$ ,  $GV$ ,  $GI$  bands and over the whole wavelength.

respectively. For more details about this network, please refer to Hortúa et al. (2020) and Zhou et al. (2022b). Our BNN is built using transfer learning technique to transfer the feature extraction part before the final output layer of CNN and then append two Bayesian layers. The weights from the transferred network are set as fixed, leveraging the features that are tailored to derive the redshift. For Bayesian layers, three common configurations are widely employed, i.e. Monte-Carlo dropout (MC-dropout, Gal & Ghahramani (2015)), flipout (Wen et al. 2018), and Multiplicative Normalizing Flows (MNF, Louizos & Welling (2017)) layer. Among these three categories, MC-dropout uses dropout to simulate varying structures of network, while the weights in flipout and MNF layers are represented by distributions. Particularly, MNF employs more complicated distributions transformed through Gaussian distribution using normalizing flows (Jimenez Rezende & Mohamed 2015). As recommended in Zhou et al. (in preparation), we adopt MNFDense layers<sup>7</sup> adapting 50

<sup>7</sup> <https://github.com/janosh/tf-mnf>

layers for masked RealNVP normalizing flow (Dinh et al. 2016). Finally, the network outputs two values, from which a Gaussian distribution representing the distribution of redshift can be derived. The illustration of architecture is also displayed in the left panel of Figure 6.

The uncertainties produced by Bayesian network must follow statistical principles that the coverage probabilities of the sample with true value within specific confidence intervals match the corresponding confidence intervals (Perreault Levasseur et al. 2017; Hortúa et al. 2020), otherwise, calibration is a necessary procedure before reporting the results. Here we employ Beta calibration technique mentioned in Kull et al. (2017) to calibrate the uncertainties.

### 3.2. Training

We only consider the spectra in  $GV$  and  $GI$  bands, since the SNRs in  $GU$  band are significantly low and the spectra are dominated by noise as shown in Figure 3 and Figure 4. Before training, our data are split into training, validation and testing sets as a ratio of 8:1:1. The number of testing set is approximately 60,000 and they are selected based on the expected redshift distribution of CSST slitless spectroscopic survey. The redshift distribution of the testing set is displayed in Figure 8, and is consistent with the one shown in Gong et al. (2019). To improve the performance of neural network, we follow the methodology in Zhou et al. (2021) to increase the size of training set by involving their Gaussian realization counterparts created through fluctuating the spectra based on the their corresponding errors. This data augmentation technique can effectively amplify the adaptability of network to the large noise in low-SNR slitless spectra. Here we use 50 random realizations. For 1d-CNN, we set loss function and optimizer as logcosh and Adam. Logcosh resembles traditional mean-absolute-error function but with a differential behavior around 0, and Adam is a stochastic gradient descent optimization method based on adaptive estimate of first-order and second-order moments (Kingma & Ba 2014). This network is trained for 100 epochs with batch size of

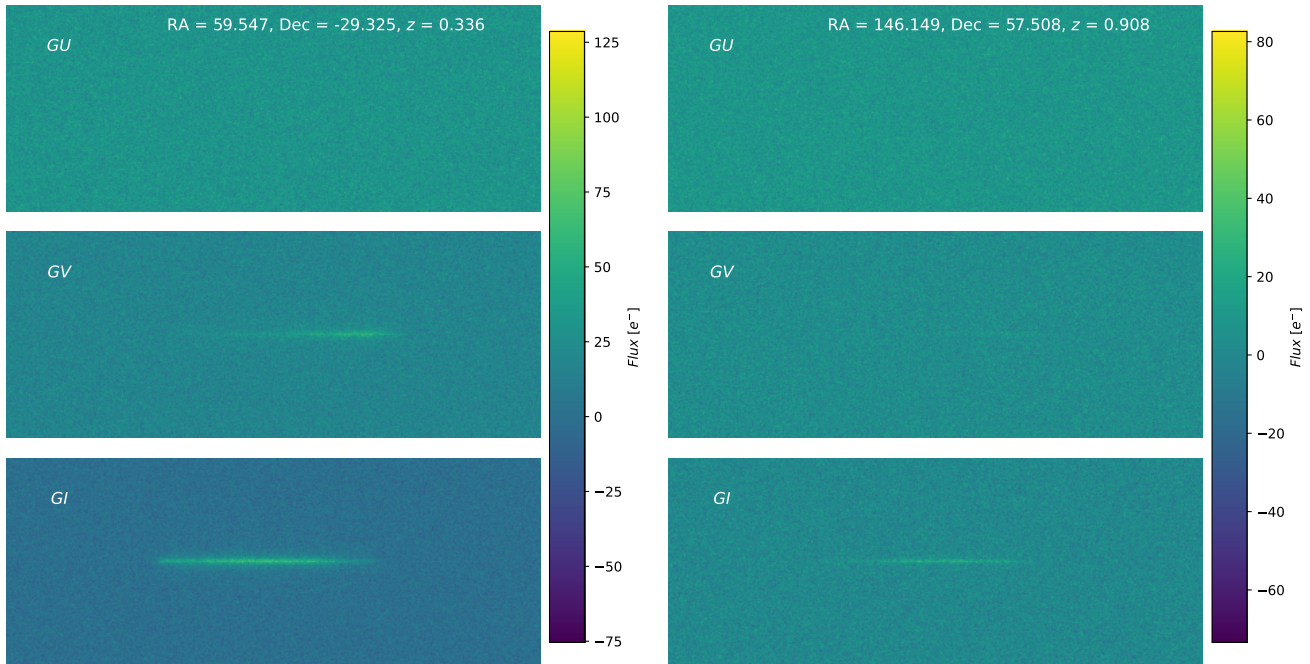


**Figure 4.** Two examples of simulated first-order slitless spectral images in *GU*, *GV* and *GI* bands. The coordinates and spectroscopic redshifts are also shown. And the corresponding extracted one-dimensional spectra and more information of the two sources are displayed in Figure 5.

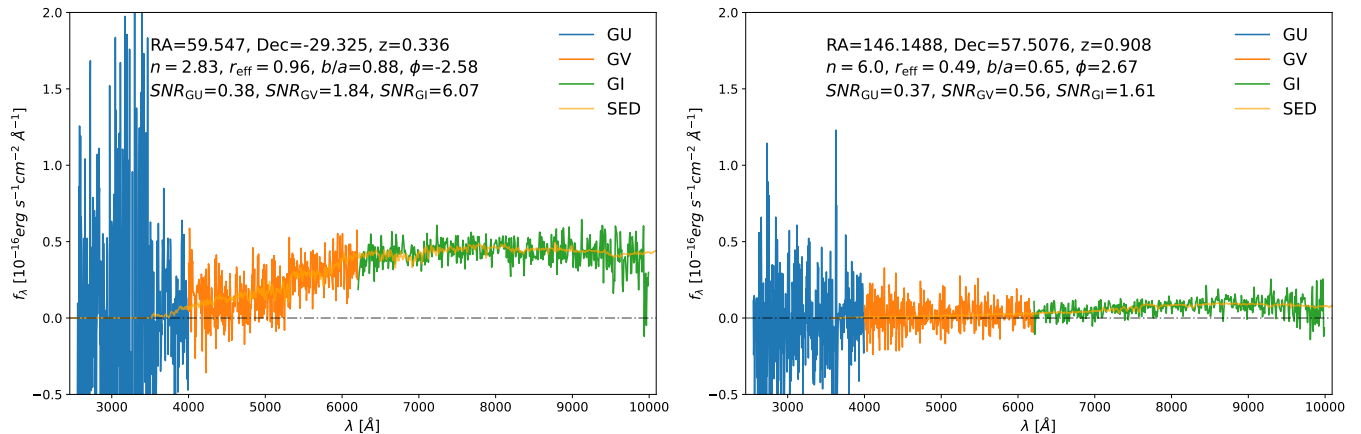


**Figure 5.** The corresponding one-dimensional spectra extracted from spectral images of sources in Figure 4. The SEDs used in simulation are also illustrated. And the black dash-dotted line indicates zero fluxes. Additionally, the source information including coordinates, spectroscopic redshifts, morphological parameters and SNR of each band are also shown.

1024 considering the graphic memory of GPU, and we select the best model with lowest loss value as our final CNN model and the backbone for BNN.

For BNN, only the weights of appended MNF layers are optimized in training. The loss function of BNN is set to be negative log-likelihood (NLL), different from the one employed in CNN, since BNN outputs a distribution considering both point values and their uncertainties. Note that the labels are solely redshift values,

since the uncertainties are naturally derived during the decrease of the loss function. Similarly, we adopt the Adam optimizer and save the model with lowest loss value. Different from the CNN in post processing, we feed the testing spectra to the BNN for 200 times. Based on these outputs, we calculate the final redshift values and their corresponding uncertainties which account for both epistemic and aleatoric ones.

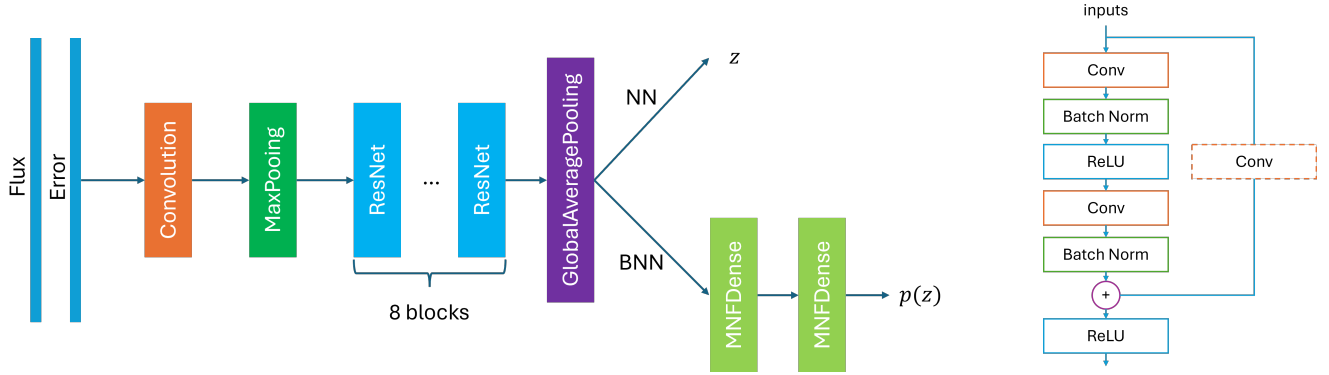


**Figure 6.** *Left:* The architecture of the 1d-CNN and BNN built upon ResNet blocks. *Right:* The structure of the ResNet block.

#### 4. RESULTS

We employ two metrics to evaluate the performance of CNN: outlier percentage  $\eta$  and normalized median absolute deviation  $\sigma_{\text{NMAD}}$ , defined as follows:

$$\eta = \frac{N_{\Delta z / (1+z_{\text{true}}) > 0.02}}{N_{\text{total}}}, \quad (4)$$

$$\sigma_{\text{NMAD}} = 1.48 \times \text{median} \left( \left| \frac{\Delta z - \text{median}(\Delta z)}{1 + z_{\text{true}}} \right| \right), \quad (5)$$

where  $\Delta z = z_{\text{pred}} - z_{\text{true}}$ , with  $z_{\text{pred}}$  and  $z_{\text{true}}$  indicating the predictions and true redshifts respectively.  $\eta$  demonstrates the fraction of severely inaccurate redshift predictions, and  $\sigma_{\text{NMAD}}$  is a robust accuracy metric that is not highly affected by the outliers.

Figure 7 illustrates the results for CNN. The accuracy  $\sigma_{\text{NMAD}}$  and outlier percentage  $\eta$  can reach 0.00047 and 0.954% respectively. The accuracy metric successfully meets the  $\sim 0.2\%$  requirement of cosmological studies for CSST. The logarithmic SNR of  $GI$  bands are also displayed by colorbar. We notice that as expected, the SNR decreases with respect to redshift and most outliers have relatively low SNR. The redshift distribution is displayed in Figure 8, and is in high consistency with true distribution. Furthermore, Figure 9 displays the accuracy and outlier percentage with respect to true redshifts in the upper and lower panel respectively. The two metrics over whole redshift range are also displayed in black dashed lines. As expected, both metrics remain steady at lower redshift and becomes worse at higher redshift.

As for the results from BNN, apart from the two metrics mentioned above, we employ another metric to measure the performance of uncertainty predictions, i.e. weighted mean uncertainty  $\bar{E}$ , which is defined as:

$$\bar{E} = \frac{\sum_i E_i / (1 + z_{i,\text{true}})}{N_{\text{total}}}, \quad (6)$$

where  $E_i$  is the uncertainty prediction for each source. The weight  $1 + z_{i,\text{true}}$  applied to each source is to elim-

inate the bias from the evolution of redshifts. The Figure 10 displays the reliability diagram for uncertainty predictions. After Beta calibration, the uncertainties better follow the statistical principle as mentioned in Section 3.1. And Figure 11 shows the results after uncertainty calibration, where the errorbars are displayed in lightblue.  $\sigma_{\text{NMAD}}$  and  $\eta$  can achieve 0.00063 and 0.92% respectively. And  $\eta$  slightly improves compared to point estimates illustrated in Figure 7, while the accuracy becomes a little worse, but still meet the requirement of cosmological studies. Furthermore, the weighed mean uncertainty  $\bar{E}$  can reach 0.00228. The redshift distribution is displayed in Figure 8, and similarly is in high consistency with true distribution. Figure 12 further analyze the behavior of uncertainties. The upper panel displays the weighted mean uncertainty  $\bar{E}$  with respect to true redshift, in which the black dashed line shows the value over the whole redshift range. As expected, this metric similarly remains stable at lower redshift and becomes worse as redshift increases. The lower panel shows the scatter plot between uncertainty and SNR in  $GI$  band, and we notice that with SNR increasing, the scatter of uncertainties becomes smaller with the values close to 0.

For comparison, according to the data analysis pipeline for CSST slitless spectra, the traditional fitting for redshift estimations may produce an accuracy as low as  $\sim 1\%$  under such low-SNR shown in Figure 3. This demonstrates that deep learning algorithm can significantly enhance the accuracy of redshift estimation from low-SNR slitless spectra.

#### 5. CONCLUSION

In this work, we employ neural network to estimate the redshift from simulated slitless spectra in the CSST slitless spectroscopic survey. The simulation requires SED and four morphological parameters including effective radius, sersic index, axis ratio and position angle of each galaxy. To simulate the slitless spectra realis-



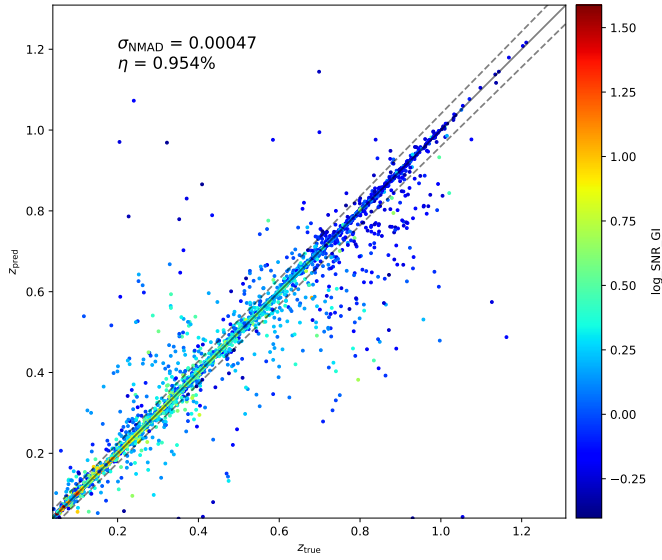


**Figure 7.** The results of 1d-CNN are illustrated, achieving accuracy  $\sigma_{\text{NMAD}} = 0.00047$  and outlier percentage  $\eta = 0.954\%$  respectively. The logarithmic SNR of *GI* bands are indicated by colorbar.

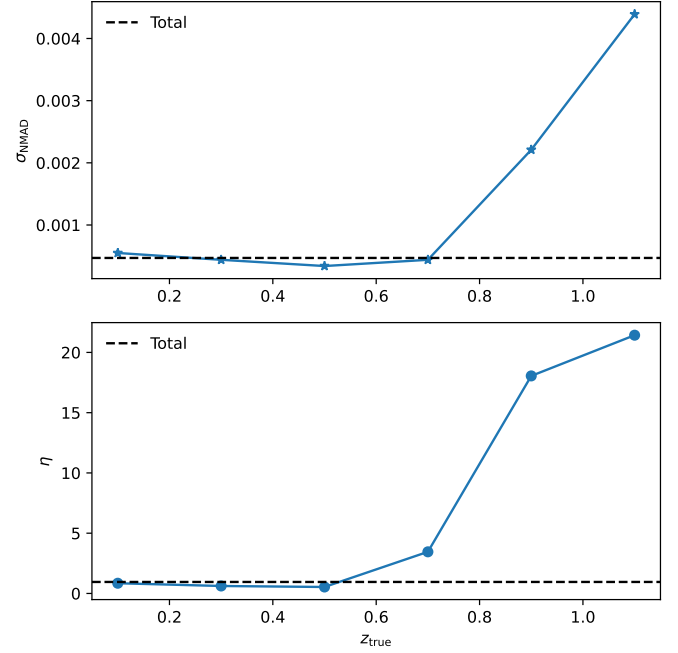


**Figure 9.** The accuracy  $\sigma_{\text{NMAD}}$  and outlier percentage  $\eta$  with respect to true redshifts are displayed in the upper and lower panel respectively. The two metrics over whole redshift range are also shown in black dashed lines.

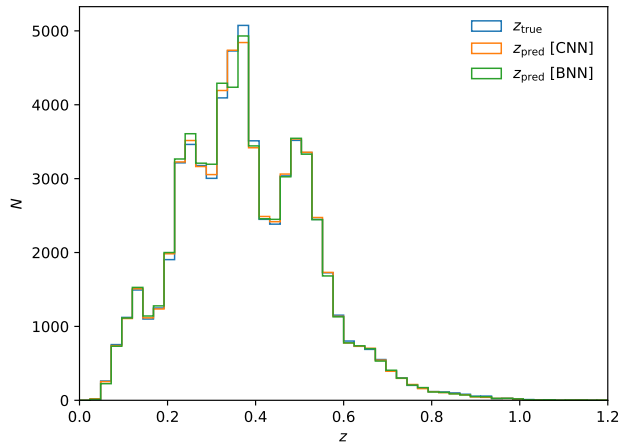


**Figure 8.** The distributions of true and predicted redshifts from CNN and BNN for testing data.

tically, we use observational data from DESI-EDR and BOSS-DR16 with high-quality spectroscopic redshifts. The model spectra generated in spectrum fitting process for these two observations are considered as SEDs, and the sources are matched with DESI LS DR9 to retrieve the required morphological parameters. The SNR of the slitless spectra are low with total SNRs peaking

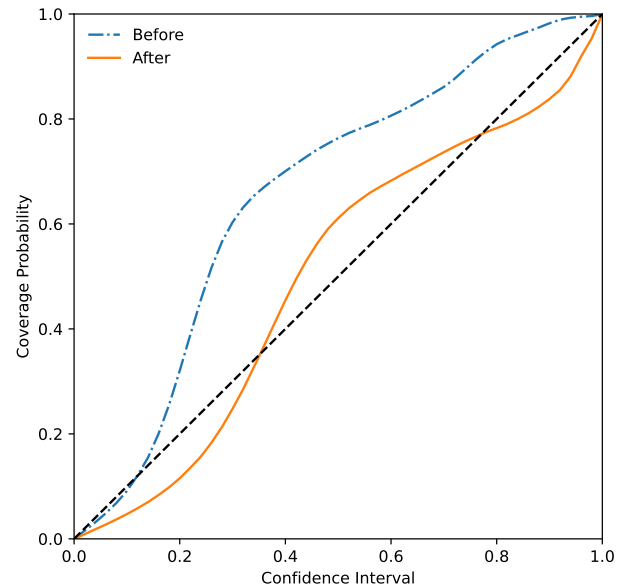


**Figure 10.** Reliability diagram for BNN results before and after the calibration. The black dashed line indicates that the uncertainties are well-calibrated with statistical principle perfectly followed.

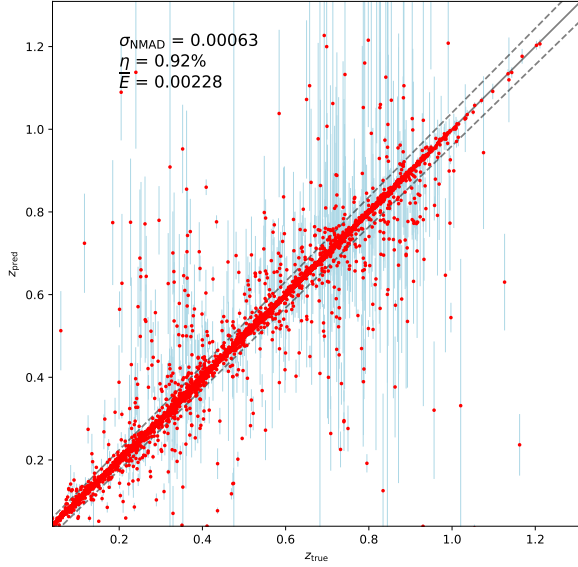


**Figure 11.** The results of BNN after uncertainty calibration. The errorbars are displayed in lightblue. Over the whole redshift range, BNN can reach  $\sigma_{\text{NMAD}} = 0.00063$  and  $\eta = 0.92\%$  respectively. And weighted mean uncertainty  $\bar{E}$  can achieve 0.00228.

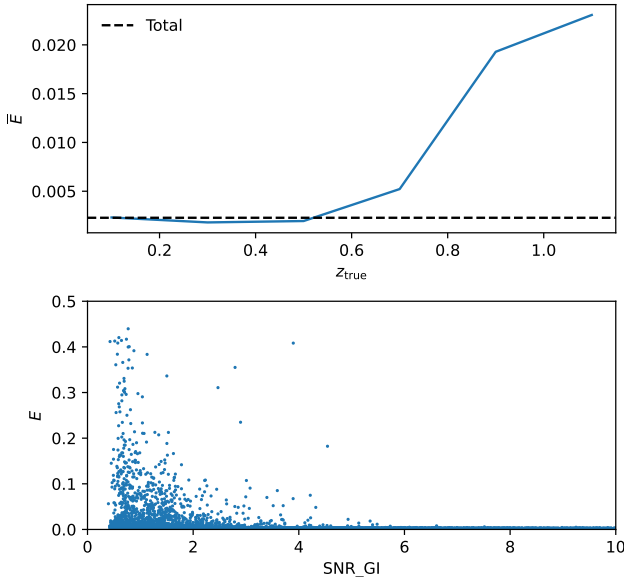


**Figure 12.** *Upper:* weighted mean uncertainty  $\bar{E}$  with respect to true redshift. The value over whole redshift range is also displayed in black dashed line. *Lower:* weighted uncertainty  $E$  with respect to SNR in *GI* band.

at  $\sim 1$ , hence the key spectroscopic features used for redshift determinations are hard to identify. Therefore, we leverage the superior capability in processing noisy data of neural network to estimate the redshifts from these slitless spectra.

Recognizing the importance of uncertainty predictions for several cosmological studies, we employ Bayesian network to accomplish this task by providing redshift estimations along with uncertainties. To increase the robustness and converging speed, we construct the BNN based on a CNN for point estimates using transfer learning techniques. Gaussian random realizations are employed to largely augment the training size, ensuring the generative ability and noise tolerance of BNN. After training, the uncertainty predictions for testing data are carefully calibrated. The BNN can achieve the results of  $\sigma_{\text{NMAD}} = 0.00063$ ,  $\eta = 0.92\%$  and  $\bar{E} = 0.00228$ , successfully satisfying the performance requirement of accuracy  $\sim 0.2\%$  for cosmological studies based on slitless spectra of CSST. Our approach can achieve better performance than traditional SED fitting, particularly for low SNR slitless spectra, serving as a complementary method for spectroscopic redshift estimation.

However, our analysis is restricted to low redshift  $z \lesssim 1$ , which can be attributed to the limitation of data from DESI-EDR and BOSS-DR16 and relatively low resolution of galaxy images from DESI legacy imaging survey. With future data release from DESI and higher resolution imaging survey, we anticipate that our simulation can reach higher redshift, better following the redshift distribution of CSST slitless spectroscopic survey, hence providing a comprehensive investigation of the spectroscopic redshift accuracy that can be achieved by deep learning algorithm.

- 1 XCZ and YG acknowledge the support from National
- 2 Key R&D Program of China grant 2022YFF0503404,
- 3 2020SKA0110402, and the CAS Project for Young Sci-
- 4 entists in Basic Research (no. YSBR-092). This work is
- 5 also supported by science research grants from the China
- 6 Manned Space Project with grant nos. CMS-CSST-
- 7 2021-B01 and CMS-CSST-2021-A01. HZ acknowledges
- 8 the science research grants from the China Manned
- 9 Space Project with Nos. CMS-CSST-2021-A02 and
- 10 CMS-CSST-2021-A04 and the supports from National
- 11 Natural Science Foundation of China (NSFC; grant
- 12 Nos. 12120101003 and 12373010) and National Key
- 13 R&D Program of China (grant Nos. 2023YFA1607800,
- 14 2022YFA1602902) and Strategic Priority Research Pro-
- 15 gram of the Chinese Academy of Science (Grant Nos.
- 16 XDB0550100).

## REFERENCES

- Agarap, A. F. 2018, arXiv e-prints, arXiv:1803.08375, doi: [10.48550/arXiv.1803.08375](https://doi.org/10.48550/arXiv.1803.08375)
- Ahumada, R., Allende Prieto, C., Almeida, A., et al. 2020, *ApJS*, 249, 3, doi: [10.3847/1538-4365/ab929e](https://doi.org/10.3847/1538-4365/ab929e)
- Arendt, A. R., Perrott, Y. C., Contreras-Santos, A., et al. 2024, *MNRAS*, 530, 20, doi: [10.1093/mnras/stae568](https://doi.org/10.1093/mnras/stae568)
- Bassett, B., & Hlozek, R. 2010, in *Dark Energy: Observational and Theoretical Approaches*, ed. P. Ruiz-Lapuente, 246, doi: [10.48550/arXiv.0910.5224](https://doi.org/10.48550/arXiv.0910.5224)
- Blundell, C., Cornebise, J., Kavukcuoglu, K., & Wierstra, D. 2015, arXiv e-prints, arXiv:1505.05424, doi: [10.48550/arXiv.1505.05424](https://doi.org/10.48550/arXiv.1505.05424)
- Busca, N., & Balland, C. 2018, arXiv e-prints, arXiv:1808.09955, doi: [10.48550/arXiv.1808.09955](https://doi.org/10.48550/arXiv.1808.09955)
- Collister, A. A., & Lahav, O. 2004, *PASP*, 116, 345, doi: [10.1086/383254](https://doi.org/10.1086/383254)
- Dawson, K. S., Schlegel, D. J., Ahn, C. P., et al. 2013, *AJ*, 145, 10, doi: [10.1088/0004-6256/145/1/10](https://doi.org/10.1088/0004-6256/145/1/10)
- DESI Collaboration, Aghamousa, A., Aguilar, J., et al. 2016, arXiv e-prints, arXiv:1611.00036, doi: [10.48550/arXiv.1611.00036](https://doi.org/10.48550/arXiv.1611.00036)
- DESI Collaboration, Adame, A. G., Aguilar, J., et al. 2023, arXiv e-prints, arXiv:2306.06308, doi: [10.48550/arXiv.2306.06308](https://doi.org/10.48550/arXiv.2306.06308)
- Dey, A., Schlegel, D. J., Lang, D., et al. 2019, *AJ*, 157, 168, doi: [10.3847/1538-3881/ab089d](https://doi.org/10.3847/1538-3881/ab089d)
- Dinh, L., Sohl-Dickstein, J., & Bengio, S. 2016, arXiv e-prints, arXiv:1605.08803, doi: [10.48550/arXiv.1605.08803](https://doi.org/10.48550/arXiv.1605.08803)
- Euclid Collaboration, Mellier, Y., Abdurro'uf, et al. 2024, arXiv e-prints, arXiv:2405.13491, doi: [10.48550/arXiv.2405.13491](https://doi.org/10.48550/arXiv.2405.13491)
- Fluri, J., Kacprzak, T., Lucchi, A., et al. 2022, *PhRvD*, 105, 083518, doi: [10.1103/PhysRevD.105.083518](https://doi.org/10.1103/PhysRevD.105.083518)
- Gal, Y., & Ghahramani, Z. 2015, arXiv e-prints, arXiv:1506.02142, doi: [10.48550/arXiv.1506.02142](https://doi.org/10.48550/arXiv.1506.02142)
- Gong, Y., Liu, X., Cao, Y., et al. 2019, *ApJ*, 883, 203, doi: [10.3847/1538-4357/ab391e](https://doi.org/10.3847/1538-4357/ab391e)
- Gupta, A., Zorrilla Matilla, J. M., Hsu, D., & Haiman, Z. 2018, *PhRvD*, 97, 103515, doi: [10.1103/PhysRevD.97.103515](https://doi.org/10.1103/PhysRevD.97.103515)
- Hamilton, A. J. S. 1998, in *Astrophysics and Space Science Library*, Vol. 231, *The Evolving Universe*, ed. D. Hamilton, 185, doi: [10.1007/978-94-011-4960-0\\_17](https://doi.org/10.1007/978-94-011-4960-0_17)
- He, K., Zhang, X., Ren, S., & Sun, J. 2015, arXiv e-prints, arXiv:1512.03385, doi: [10.48550/arXiv.1512.03385](https://doi.org/10.48550/arXiv.1512.03385)
- He, Z., Er, X., Long, Q., et al. 2020, *MNRAS*, 497, 556, doi: [10.1093/mnras/staa1917](https://doi.org/10.1093/mnras/staa1917)
- Henghes, B., Thiyaalingam, J., Pettitt, C., Hey, T., & Lahav, O. 2022, *MNRAS*, 512, 1696, doi: [10.1093/mnras/stac480](https://doi.org/10.1093/mnras/stac480)
- Hortúa, H. J., García, L. Á., & Castañeda C., L. 2023, *Frontiers in Astronomy and Space Sciences*, 10, 1139120, doi: [10.3389/fspas.2023.1139120](https://doi.org/10.3389/fspas.2023.1139120)
- Hortúa, H. J., Volpi, R., Marinelli, D., & Malagò, L. 2020, *PhRvD*, 102, 103509, doi: [10.1103/PhysRevD.102.103509](https://doi.org/10.1103/PhysRevD.102.103509)
- Ioffe, S., & Szegedy, C. 2015, arXiv e-prints, arXiv:1502.03167, doi: [10.48550/arXiv.1502.03167](https://doi.org/10.48550/arXiv.1502.03167)
- Jimenez Rezende, D., & Mohamed, S. 2015, arXiv e-prints, arXiv:1505.05770, doi: [10.48550/arXiv.1505.05770](https://doi.org/10.48550/arXiv.1505.05770)
- Kingma, D. P., & Ba, J. 2014, arXiv e-prints, arXiv:1412.6980, doi: [10.48550/arXiv.1412.6980](https://doi.org/10.48550/arXiv.1412.6980)
- Kull, M., Filho, T. S., & Flach, P. 2017, in *Proceedings of Machine Learning Research*, Vol. 54, *Proceedings of the 20th International Conference on Artificial Intelligence and Statistics*, ed. A. Singh & J. Zhu (PMLR), 623–631. <https://proceedings.mlr.press/v54/kull17a.html>
- Le Fevre, O., Cassata, P., Cucciati, O., et al. 2013, arXiv e-prints, arXiv:1307.0545, doi: [10.48550/arXiv.1307.0545](https://doi.org/10.48550/arXiv.1307.0545)
- Lecun, Y., Bottou, L., Bengio, Y., & Haffner, P. 1998, *Proceedings of the IEEE*, 86, 2278, doi: [10.1109/5.726791](https://doi.org/10.1109/5.726791)
- Li, R., Napolitano, N. R., Tortora, C., et al. 2020, *ApJ*, 899, 30, doi: [10.3847/1538-4357/ab9dfa](https://doi.org/10.3847/1538-4357/ab9dfa)
- Lilly, S. J., Le Fevre, O., Renzini, A., Zamorani, G., & Scodreggio, M. 2007, *ApJS*, 172, 70, doi: [10.1086/516589](https://doi.org/10.1086/516589)
- Louizos, C., & Welling, M. 2017, arXiv e-prints, arXiv:1703.01961, doi: [10.48550/arXiv.1703.01961](https://doi.org/10.48550/arXiv.1703.01961)
- MacKay, D. J. C. 1995, *Network: Computation in Neural Systems*, 6, 469
- Mainieri, V., Anderson, R. I., Brinchmann, J., et al. 2024, arXiv e-prints, arXiv:2403.05398, doi: [10.48550/arXiv.2403.05398](https://doi.org/10.48550/arXiv.2403.05398)
- Min, Z., Xiao, X., Ding, J., et al. 2024, arXiv e-prints, arXiv:2404.09483, doi: [10.48550/arXiv.2404.09483](https://doi.org/10.48550/arXiv.2404.09483)
- Pan, S., Liu, M., Forero-Romero, J., et al. 2020, *Science China Physics, Mechanics, and Astronomy*, 63, 110412, doi: [10.1007/s11433-020-1586-3](https://doi.org/10.1007/s11433-020-1586-3)
- Pasquet, J., Bertin, E., Treyer, M., Arnouts, S., & Fouchez, D. 2019, *A&A*, 621, A26, doi: [10.1051/0004-6361/201833617](https://doi.org/10.1051/0004-6361/201833617)
- Pearson, W. J., Wang, L., Trayford, J. W., Petrillo, C. E., & van der Tak, F. F. S. 2019, *A&A*, 626, A49, doi: [10.1051/0004-6361/201935355](https://doi.org/10.1051/0004-6361/201935355)
- Perreault Levasseur, L., Hezaveh, Y. D., & Wechsler, R. H. 2017, *ApJL*, 850, L7, doi: [10.3847/2041-8213/aa9704](https://doi.org/10.3847/2041-8213/aa9704)

- Rastegarnia, F., Mirtorabi, M. T., Moradi, R., Vafaei Sadr, A., & Wang, Y. 2022, MNRAS, 511, 4490, doi: [10.1093/mnras/stac076](https://doi.org/10.1093/mnras/stac076)
- Rezaei, S., McKean, J. P., Biehl, M., de Roo, W., & Lafontaine, A. 2022, MNRAS, 517, 1156, doi: [10.1093/mnras/stac2078](https://doi.org/10.1093/mnras/stac2078)
- Sabelhaus, P. A., & Decker, J. E. 2004, in Society of Photo-Optical Instrumentation Engineers (SPIE) Conference Series, Vol. 5487, Optical, Infrared, and Millimeter Space Telescopes, ed. J. C. Mather, 550–563, doi: [10.1117/12.549895](https://doi.org/10.1117/12.549895)
- Sadeh, I. 2014, in Statistical Challenges in 21st Century Cosmology, ed. A. Heavens, J.-L. Starck, & A. Krone-Martins, Vol. 306, 316–318, doi: [10.1017/S1743921314010849](https://doi.org/10.1017/S1743921314010849)
- Schaefer, C., Geiger, M., Kuntzer, T., & Kneib, J. P. 2018, A&A, 611, A2, doi: [10.1051/0004-6361/201731201](https://doi.org/10.1051/0004-6361/201731201)
- Schlegel, D. J., Kollmeier, J. A., Aldering, G., et al. 2022, arXiv e-prints, arXiv:2209.04322, doi: [10.48550/arXiv.2209.04322](https://doi.org/10.48550/arXiv.2209.04322)
- Srivastava, N., Hinton, G., Krizhevsky, A., Sutskever, I., & Salakhutdinov, R. 2014, Journal of Machine Learning Research, 15, 1929. <http://jmlr.org/papers/v15/srivastava14a.html>
- Tamura, N., Takato, N., Shimono, A., et al. 2016, in Society of Photo-Optical Instrumentation Engineers (SPIE) Conference Series, Vol. 9908, Ground-based and Airborne Instrumentation for Astronomy VI, ed. C. J. Evans, L. Simard, & H. Takami, 99081M, doi: [10.1117/12.2232103](https://doi.org/10.1117/12.2232103)
- Tewes, M., Kuntzer, T., Nakajima, R., et al. 2019, A&A, 621, A36, doi: [10.1051/0004-6361/201833775](https://doi.org/10.1051/0004-6361/201833775)
- Wen, Y., Vicol, P., Ba, J., Tran, D., & Grosse, R. 2018, arXiv e-prints, arXiv:1803.04386, doi: [10.48550/arXiv.1803.04386](https://doi.org/10.48550/arXiv.1803.04386)
- Zhan, H. 2018, in 42nd COSPAR Scientific Assembly, Vol. 42, E1.16–4–18
- Zhang, Z., Shan, H., Li, N., et al. 2024, A&A, 683, A209, doi: [10.1051/0004-6361/202345903](https://doi.org/10.1051/0004-6361/202345903)
- Zhou, X., Gong, Y., Meng, X.-M., et al. 2022a, Research in Astronomy and Astrophysics, 22, 115017, doi: [10.1088/1674-4527/ac9578](https://doi.org/10.1088/1674-4527/ac9578)
- . 2022b, Research in Astronomy and Astrophysics, 22, 115017, doi: [10.1088/1674-4527/ac9578](https://doi.org/10.1088/1674-4527/ac9578)
- . 2021, ApJ, 909, 53, doi: [10.3847/1538-4357/abda3e](https://doi.org/10.3847/1538-4357/abda3e)